A New Technique for Endobronchial Ultrasonography and Comparison of Two Ultrasonic Probes*

Analysis With a Plot Profile of the Image Analysis Software NIH Image

Yoshihiro Nakamura, MD; Chiaki Endo, MD; Masami Sato, MD, FCCP; Akira Sakurada, MD; Shun-ichi Watanabe, MD; Ryuzo Sakata, MD; and Takashi Kondo, MD

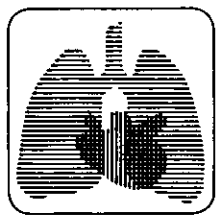

Vol. 126, p. 192-197
July 2004 Issue

Reprinted from CHEST

A New Technique for Endobronchial Ultrasonography and Comparison of Two Ultrasonic Probes*

Analysis With a Plot Profile of the Image Analysis Software NIH Image

Yoshihiro Nakamura, MD; Chiaki Endo, MD; Masami Sato, MD, FCCP; Akira Sakurada, MD; Shun-ichi Watanabe, MD; Ryuzo Sakata, MD; and Takashi Kondo, MD

Study objectives: **Endobronchial ultrasonography (EBUS) is currently the sole clinical method available for delineating the bronchial wall structure; however, the image resolution is inadequate. Thus, an improved image analysis system is needed for both a more accurate and more readily interpretable endobronchial ultrasonogram.**

Materials and methods: **A total of 10 patients underwent pulmonary resection for lung cancer. EBUS was performed on the bronchi of the resected lungs, which had been immersed in physiologic saline solution. The same bronchial lesion in each specimen was imaged with two probes: 20 MHz and 30 MHz. The images were analyzed using the plot profile derived from freeware image analysis software: NIH Image (National Institutes of Health; Bethesda, MD). The measured echo intensity of the bronchial wall was statistically analyzed.**

Results: **A normal bronchial wall image consists of five layers, and the plot profile shows a W-shaped curve. The mean value of the echo intensity of each peak or trough of the W-shaped curve was calculated and compared for both probes. The differences in the mean echo intensity between both the third and fourth layer and the second and fourth layer were found to be significantly greater with the 30-MHz probe than with the 20-MHz probe. The echo intensity curve of a central-type lung cancer was not W shaped, indicating that the bronchial wall was not composed of the normal five layers.**

Conclusion: **We employed image analysis software and drew a plot to obtain a W-shaped curve from the EBUS image data. This enabled us to make an objective assessment of the laminar structure of the bronchial wall. In order to clearly recognize the laminar structure of the bronchial wall, the 30-MHz probe was found to be more useful than the 20-MHz probe.**

(CHEST 2004; 126:192–197)

Key words: bronchial wall invasion; central-type lung cancer; endobronchial ultrasonography; image analysis

Abbreviations: EBUS = endobronchial ultrasonography; PDT = photodynamic therapy

The laminar structure of the bronchial wall as visualized by endobronchial ultrasonography (EBUS) was first described by Hurter and Hanrath[1] in 1992. Subsequently, a number of studies[2-9] have been conducted, suggesting that EBUS might be useful for imaging the laminar structure of the bronchial wall and evaluating the depth of tumor invasion in central-type bronchogenic carcinoma. EBUS is currently the sole method available for delineating the bronchial wall structure in the clinical setting; however, the image resolution is inadequate for the attainment of a clear laminated view of the bronchial wall, which has a maximum thickness of approximately 5 mm. A learning curve is required for the ultrasonic evaluation of the extent of tumor invasion into the bronchial wall. Even experienced interpreters have to rely on their subjective judgment. For more accurate and simpler interpretation,

*From the Department of Surgery (Drs. Nakamura, Watanabe, and Sakata), Faculty of Medicine, Kagoshima University, Kagoshima; and Department of Thoracic Surgery (Drs. Endo, Sato, Sakurada, and Kondo), Institute of Development, Aging and Cancer Tohoku University, Sendai, Japan.

Manuscript received June 19, 2003; revision accepted February 4, 2004.

Correspondence to: Chiaki Endo, MD, Department of Thoracic Surgery, Institute of Development, Aging and Cancer, Tohoku University, 4-1 Seiryomachi, Aoba-ku, Sendai 980-8575, Japan; e-mail: endo@idac.tohoku.ac.jp

we employed an image analysis system for EBUS that enabled us to acquire a clear laminated view of the bronchial wall and make an objective assessment of the feasibility of echo probes and the extent of tumor invasion *ex vivo*.

Materials and Methods

Materials

From February through March 2002, 10 patients underwent pulmonary resection for lung cancer. The operative procedure was a pneumonectomy in one case, a sleeve lobectomy in two cases, and a lobectomy in seven cases. The resected lung specimens were used for this study. The specimens were immersed in physiologic saline solution within 1 hour of the resection, in order to prevent autolytic changes and to obtain high-quality ultrasonic images without interference from air. The EBUS system used in this study was manufactured by Olympus (Tokyo, Japan), and had the following specifications: an EU-M 30 processor; a UM-BS20–26R ultrasonic probe (20-MHz radial scanner; rotation rate, 400/s); a XUM-BS30–26R ultrasonic probe (30-MHz radial scanner; rotation rate, 400/s); and a MAJ-643R (latex balloon sheath; outer diameter, 2.6 mm). The balloon sheath of the ultrasonic probe was filled with physiologic saline solution.

EBUS Procedure

EBUS was performed on the bronchus of the resected lung within 1 h of the resection. During the EBUS procedure, the resected lung was immersed in physiologic saline solution. First, the ultrasonic probe with the balloon sheath was inserted into the bronchial lumen. Second, the balloon sheath was expanded with physiologic saline solution until the lumen was obstructed. Third, EBUS images of the bronchus were captured after adjusting the brightness and contrast of the images (Fig 1). The same bronchial lesion in each specimen was observed using two different types of probes: 20 MHz and 30 MHz.

With the use of the balloon sheath, the study conditions were similar to the actual conditions in EBUS. When we perform EBUS in actual patients, the ultrasonic probe is used with the balloon sheath; for this reason, the balloon sheath was used in this study, although clearer images can be obtained if the EBUS is performed without the balloon sheath.

Image Analysis

The captured ultrasonogram was analyzed using freeware image analysis software (NIH Image, Version 1.62; National Institutes of Health; Bethesda, MD).[10] The plot profile of the NIH Image was used, and the echo intensity of the ultrasonogram was measured. When an echo image was pure white (hyperechoic) in the ultrasonogram, the plot profile indicated 256 pixels; when it was pure black (hypoechoic), it indicated 0 pixels.

First, a radial line from the ultrasonic probe was drawn on the ultrasonogram, which perpendicularly intersected the bronchial wall. Second, the echo intensity on the line was plotted, and the plotted data on the total length of the line were obtained. Finally, we obtained the echo intensity curve as shown in Figure 2, *top*. Normally, the bronchial wall consists of five layers in an ultrasonogram: an innermost hyperechoic layer representing the balloon latex sheath and the bronchial epithelium; a hypoechoic second layer representing the submucosal layer; a hyperechoic third layer, which represents the marginal echo of the bronchial cartilaginous layer; a hypoechoic fourth layer representing the bronchial cartilaginous layer; and the outer most hyperechoic fifth layer representing the marginal echo of the outer cartilaginous layer and the outer margin of the bronchial wall. Therefore, the echo intensity curve is W shaped. The longitudinal axis represents the echo intensity, and the horizontal axis represents the distance from the ultrasonic probe.

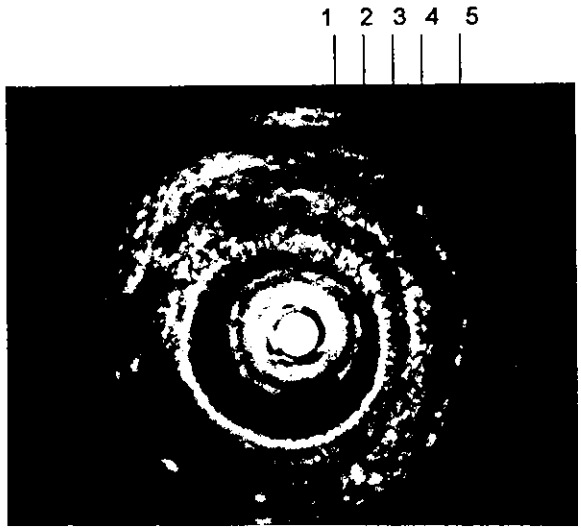

FIGURE 1. Representative endobronchial ultrasonogram showing a laminar structure of the bronchial wall. A central circular lesion is an echo probe, and a five-layer laminar structure is depicted. The first lamina is a hyperechoic layer representing the balloon sheath and the bronchial epithelium; the second lamina is hypoechoic layer representing the submucosal layer and the bronchial smooth-muscle layer; the third lamina is a hyperechoic layer representing the marginal echo of the luminal aspect of the bronchial cartilaginous layer; the fourth lamina is a hypoechoic layer representing the bronchial cartilaginous layer; and the outermost (fifth) lamina is composed of a hyperechoic layer representing the marginal echo of the outer cartilaginous layer and the outer margin of the bronchial wall. Numbered arrows indicate the layers of the bronchial wall as mentioned above.

The analysis was made of the image displayed on the monitor. The pixel values altered when the brightness of the image was changed. However, these alterations did not influence the results of the image analysis. First, each lamina has to be distinguished from the others in order to clearly recognize the laminar structure of the bronchial wall. If the difference of the pixel values between laminae increases, we can more clearly recognize the laminar structure. Accordingly, the most important thing to clearly recognize the laminar structure is not the pixel values of each lamina but the difference in pixel values between laminae. Furthermore, the differences of the pixel values between peaks and troughs did not vary even if the brightness of the image was changed. Because the change of each pixel value was the same as other values, the difference in the pixel values was constant.

Second, if we compare the performance of two ultrasound probes, each ultrasound image had to be obtained under the optimal conditions of that probe; specifically, each image must be obtained by the ultrasound probe, which is in accordance with its performance characteristics. The optimal conditions for one

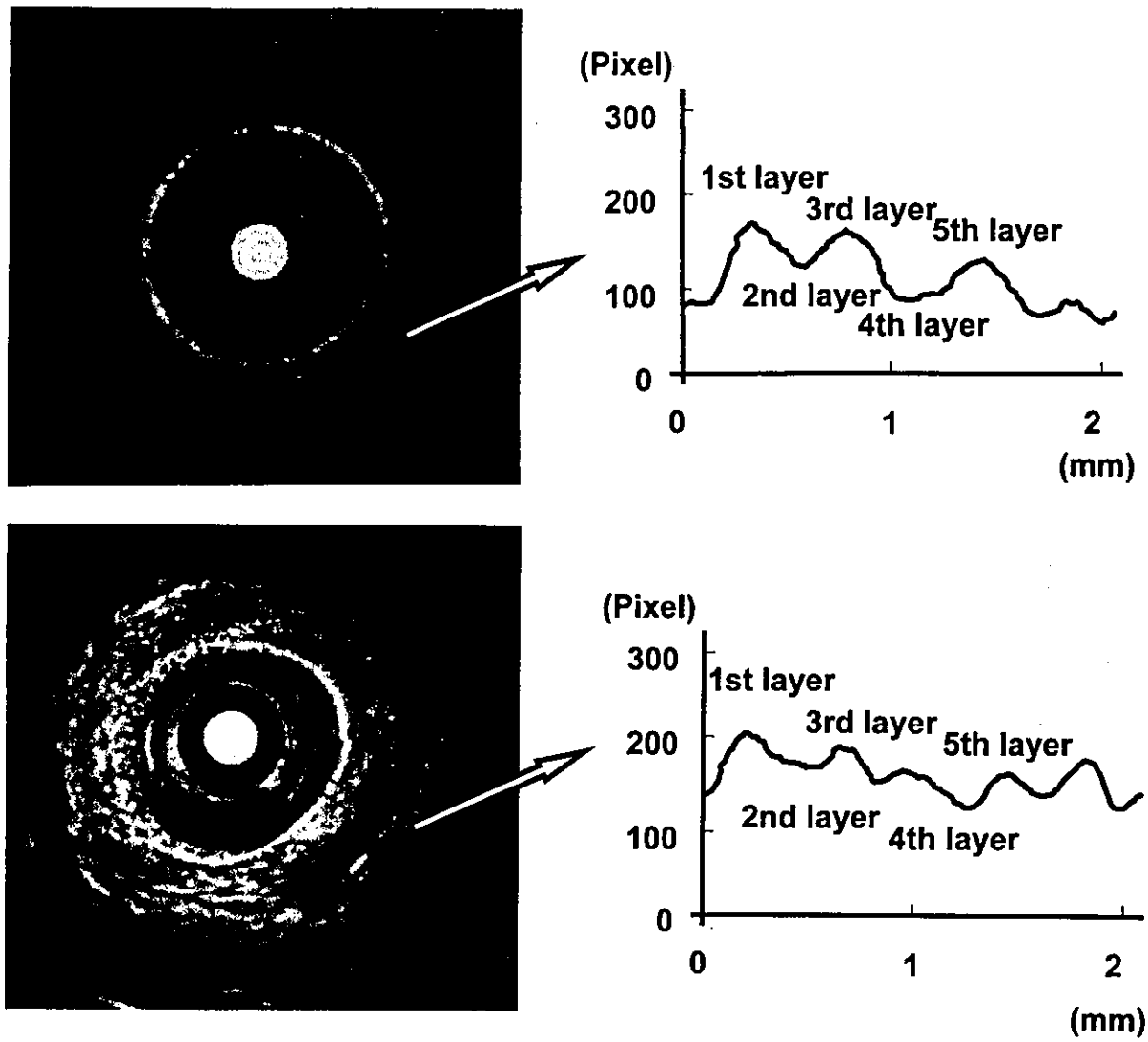

FIGURE 2. EBUS was performed at the same site of the bronchus with two kinds of ultrasonic probes, and ultrasonograms and their accompanying echo intensity curves were obtained (*top*, 30-MHz probe; *bottom*, 20-MHz probe). It would be subjectively understood that the ultrasonogram of the 30-MHz probe (*top*) shows higher resolution than that of the 20-MHz probe (*bottom*). However, the five-layer laminar structure might not be seen easily with the direct evaluation of the ultrasonogram. However, image analysis with NIH Image shows bronchial laminar structure as a W-shaped curve. An open rectangular lesion is analyzed with plot profile of NIH Image, and a certain plot of the rectangle is assigned from 0 to 256 pixels, according to its echo intensity. A W-shaped curve indicates a five-layer laminar structure of the bronchial wall. Echo intensity is plotted on the y-axis, and the distance from the echo probe is shown on the x-axis. Furthermore, the echo intensity curve of the 30-MHz probe shows steeper W-shaped curve than that of the 20-MHz probe. That is, the difference between peak and trough of the echo intensity curve is larger with the 30-MHz probe than the 20-MHz probe, and objectively shows that the 30-MHz probe has higher resolution than the 20-MHz probe.

ultrasound probe may be different than those for the other probe. We had to adjust the brightness of the image each time in order to obtain its optimal conditions.

Statistical Analysis

The measured echo intensity of the bronchial wall was statistically analyzed. The W-shaped echo intensity curve has five peaks and troughs, and each peak or trough represents the echo intensity of the most hyper or hypoechoic lesion in the corresponding layer of the laminar structure of the bronchial wall. The mean value of each peak or trough of the echo intensity curve of all specimens was calculated, and statistical comparison was conducted. The paired *t* test was used to compare the echo intensities, and $p < 0.05$ was considered as denoting significance. Informed consent was obtained from all patients before they were entered into the study group.

Results

A total of 10 normal bronchi from 10 patients with lung cancer were examined. Figure 2 presents ultrasonograms and echo intensity curves, which were obtained at the same site of the normal bronchus by two different ultrasonic probes: 30 MHz and 20 MHz. It is common knowledge that the ultrasonogram obtained with a 30-MHz probe (Fig 2, *top*) exhibits a higher resolution than that obtained with a 20-MHz probe (Fig 2, *bottom*). However, five layers of laminar structure might not be readily seen by direct assessment of the ultrasonograms. Conversely, the echo intensity curves showed five peaks and troughs, indicating that the normal bronchial wall is a laminar structure consisting of five ultrasonically distinct layers. Moreover, the echo intensity curve of Figure 2, *top*, showed a steeper W-shaped curve than that of Figure 2, *bottom*; specifically, the difference between the peak and trough of the echo intensity curve is greater with the 30-MHz probe than it is with the 20-MHz probe. This finding objectively demonstrates that the 30-MHz probe has a higher resolution than the 20-MHz probe. Figure 3 shows the mean value of the echo intensity of each layer of the laminar structure of the bronchial wall, obtained with different ultrasonic probes: 20 MHz and 30 MHz. Figure 4 shows the difference in the mean echo intensity between the third and fourth layer as well as the second and fourth layer using two different ultrasonic probes. The differences were found to be significantly greater with the 30-MHz probe than with the 20-MHz probe. Figure 5 shows the echo intensity curve of a central-type bronchogenic squamous cell carcinoma. This curve is not W

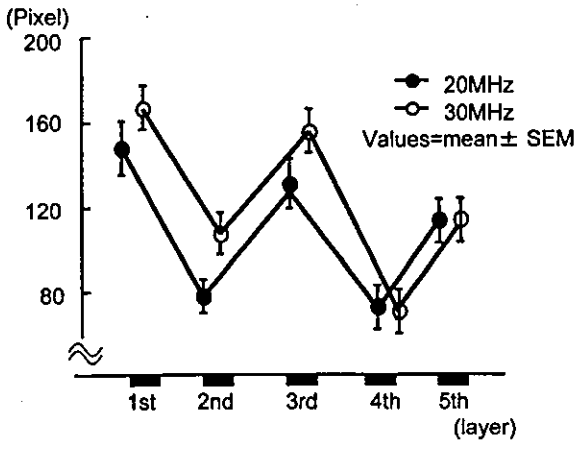

FIGURE 3. Mean value of echo intensity of each layer of the laminar structure of the normal bronchial wall of 10 patients with lung cancer using the 20-MHz (closed circle) and 30-MHz (open circle) echo probes.

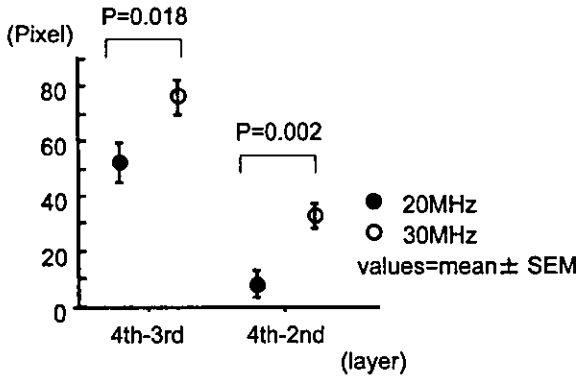

FIGURE 4. The difference in the mean echo intensity between the third and fourth layer and the second and fourth layer using the two types of echo probes. The difference is found to be significantly greater with the 30-MHz probe than with the 20-MHz probe.

shaped, indicating that the bronchial wall is not composed of the normal five layers and the tumor has invaded beyond the bronchial wall.

Discussion

In almost all reports discussing EBUS, the ultrasound images were compared using subjective evaluation; thus, the results might vary between examiners. For example, when one examiner states that a particular bronchial wall consists of four layers, another may state that it has five layers. When one examiner states that a tumor has invaded beyond the cartilaginous layer, another might state that the tumor is within the cartilaginous layer. When one examiner states that a particular image is clearer than another, a different examiner might state the reverse. These discrepancies are due to inadequate image resolution. If EBUS had a resolution as fine as abdominal ultrasonography, all examiners would arrive at the same conclusion, merely by subjectively evaluating the raw image data.

In cases with early central-type lung cancer, it may be essential for making the appropriate therapeutic decision to know the depth of tumor invasion into the bronchial wall at the laminar level. When a tumor penetrates the cartilaginous layer, photodynamic therapy (PDT) may no longer effective.[8,11–14] To obtain an optimal therapeutic outcome, the physician needs to know whether the lesion has invaded the cartilaginous layer. Currently, EBUS is the only clinically available method for imaging the laminar structure of the bronchial wall; however, the currently available EBUS apparatus does not yield a sharp enough image to permit accurate evaluation of the depth of tumor invasion into the bronchial wall.

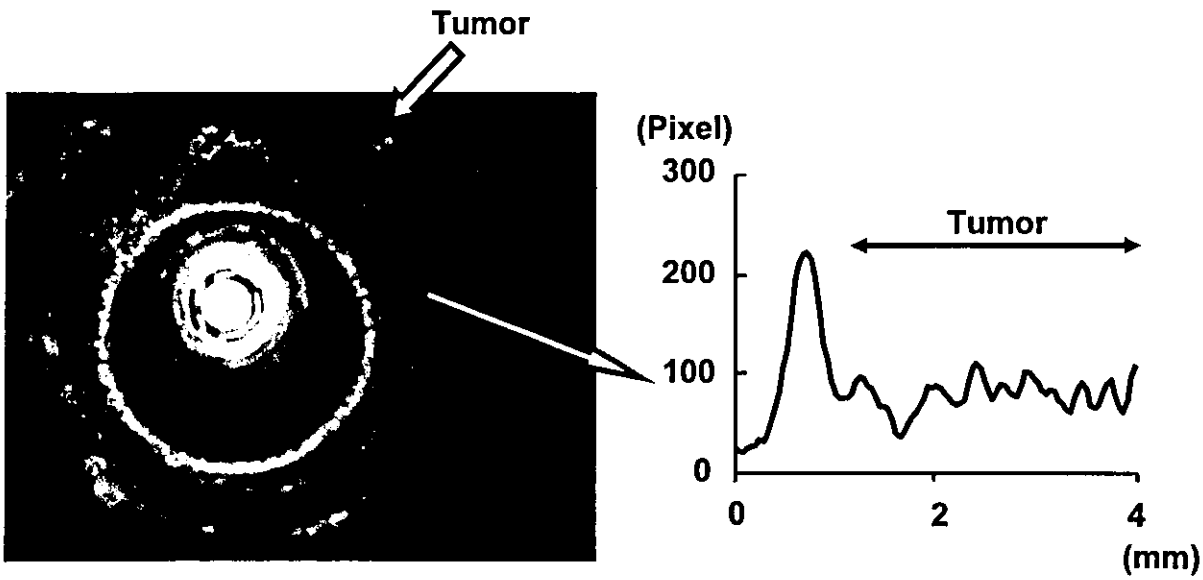

FIGURE 5. Representative endobronchial ultrasonogram showing an endobronchial tumor. A white dotted line shows the margin of the tumor. The image analysis with NIH Image shows a curve that is completely different from the W-shaped curve. This means that the tumor has extrabronchial wall invasion.

In this study, we employed image analysis software to digitize the EBUS image. This allowed us to draw a plot of the EBUS data from the bronchial wall and perform statistical analysis for an objective assessment. The laminar structure of the normal bronchial wall is represented by a 5-point W-shaped curve, from which the status of each layer can be estimated. When the digitized data did not form a W-shaped curve in this study, the bronchial wall was considered to be abnormal and presence of a tumor or other lesion was assumed. The degree of deviation from W-shaped curve reflected the extent of lesion invasion into the bronchial wall.

Few studies[9,15] have subjectively compared the image quality of the bronchial wall layers using EBUS transducer probes of different frequencies. In this study, we examined the ultrasound images of the bronchial wall structure using both the 20-MHz and 30-MHz transducers. The ultrasound image data were digitized, and the images were statistically compared. The results revealed that the 30-MHz transducer was significantly more useful for delineating the bronchial wall layers than the 20-MHz probe. The 30-MHz transducer achieved excellent results, particularly in regard to the echo contrast between the second and fourth layers as well as between the third and fourth layers. For therapeutic decisions for to use PDT, it is crucial to determine whether the fourth layer is invaded by the tumor; the 30-MHz transducer appeared to be significantly superior to the 20-MHz transducer for the assessment of the extent of tumor invasion into the bronchial wall.

In summary, EBUS has been used commonly in the assessment of tumor invasion in early central-type lung cancers.[2–9] However, it is often difficult to interpret the ultrasound images of the bronchial wall, which has a maximal thickness of 5 mm, and consists of five layers. Although accurate evaluation of tumor invasion of the fourth (cartilaginous) layer is required for a therapeutic decision for PDT or other treatment modalities, raw ultrasound images are often too unclear to distinguish each layer. In this study, we employed image analysis software and drew a plot to obtain a W-shaped curve from the EBUS image data. This enabled us to make an objective assessment of the laminar structure of the bronchial wall. Data distribution also showed a significant difference in the delineation of the bronchial wall structure between the two transducers: 20 MHz and 30 MHz. Our image analysis is an objective evaluation, and any examiner should arrive at the same results. If we cannot clearly image the laminar structure, we cannot accurately evaluate the extent of tumor invasion. For therapeutic decisions for PDT, evaluation of tumor invasion of the fourth layer (the cartilaginous layer) is considered to be crucial. We cannot perform PDT effectively if the tumor has invaded beyond the cartilaginous layer. In this study, we showed the statistically significant superiority of the 30-MHz probe in the imaging of the laminar

structure of the bronchial wall. Specifically, by using the 30-MHz probe, we can more accurately image the cartilaginous layer. Accordingly, the 30-MHz probe was found to be more useful than the 20-MHz probe for recognition of the extent of tumor invasion into the bronchial wall. Until a high-resolution EBUS system permitting direct assessment of an ultrasonogram of the bronchial wall is developed, our approach should remain useful for the detection and evaluation of the laminar structure of the bronchial wall and the extent of tumor invasion. Our image analysis is an objective evaluation, and any examiner should arrive at the same results. Our next goal is to apply this analytical method to EBUS data in clinical practice.

ACKNOWLEDGMENT: The authors wish to thank to Mr. Hirooka and Mr. Nishina (Olympus Co. Ltd.) for technical assistance.

REFERENCES

1 Hurter T, Hanrath P. Endobronchial sonography: feasibility and preliminary results. Thorax 1992; 47:565–567
2 Becker HD. Endobronchialer Ultraschall-Eine neue Perspektive in der Bronchologie. Ultraschall Med 1996; 17:106–112
3 Kurimoto N, Murayama M, Yoshioka S, et al. Assessment of usefulness of endobronchial ultrasonography in determination of depth of tracheobronchial tumor invasion. Chest 1999; 115:1500–1506
4 Lam S, Becker HD. Thoracic endoscopy: future diagnostic procedures. Chest Surg Clin North Am 1996; 6:363–379
5 Tanaka F, Muro K, Yamasaki S, et al. Evaluation of tracheobronchial wall invasion using transbronchial ultrasonography (TBUS). Eur J Cardiothorac Surg 2000; 17:570–574
6 Baba M, Sekine Y, Suzuki M, et al. Correlation between endobronchial ultrasonography (EBUS) images and histologic findings in normal and tumor-invaded bronchial wall. Lung Cancer 2002; 35:65–71
7 Yoshimura H, Kida A, Arai T, et al. Bronchology and bronchoesophagology: state of the art. Amsterdam, the Netherlands: Elsevier Science, 2001; 411–414
8 Miyazu Y, Miyazawa T, Kurimoto N, et al. Endobronchial ultrasonography in the assessment of centrally located early-stage lung cancer before photodynamic therapy. Am J Respir Crit Care Med 2002; 165:832–837
9 Kurimoto N, Murayama M, Nishisaka T, et al. Advances in determination of the depth of tumor invasion of tracheobronchial wall using a 30 MHz probe and 3D endobronchial ultrasonography. J Jpn Soc Bronchol 2002; 24:375–378
10 About NIH Image. Bethesda, MD: National Institutes of Health. Available at: http://rsb.info.nih.gov/nih-image/. Accessed June 9, 2004
11 Sutedja G, Postmus PE. Bronchoscopic treatment of lung tumors. Lung Cancer 1994; 11:1–17
11 Seijo LM, Sterman DH. Interventional pulmology. N Engl J Med 2001; 344:740–749
12 Fujimura S, Sakurada A, Sagawa M, et al. A therapeutic approach to roentgenographically occult squamous cell carcinoma of the lung. Cancer 2000; 89:2445–2448
13 Saito Y, Nagamoto N, Ota S, et al. Results of surgical treatment for roentgenographically occult bronchogenic squamous cell carcinoma. J Thorac Cardiovasc Surg 1992; 104:401–407
14 Dong B, Takahashi H, Sagawa M, et al. Comparison of ultrasonographical images obtained by three different types of ultrasonic probes. J Jpn Soc Bronchol 2001; 23:104–108

Directions of Mucous Surface Waves in Large Bronchi Are Different Between Human Beings and Quadrupeds

Yoshihiro Nakamura, MD,† Akira Sakurada, MD,* Masami Sato, MD,* Chiaki Endo, MD,* Shun-ichi Watanabe, MD,† Ryuzo Sakata, MD,† and Takashi Kondo, MD**

Abstract: The purpose of this study was to investigate the directions of mucous surface waves and mucous flow in the large bronchi. The materials were tracheae, carinae, and main bronchi of 12 humans, 5 pigs, 3 monkeys, and 1 rabbit. Mucous surface waves and mucous flow were observed with a stereoscopic zoom microscope system. Large differences in the directions of mucous surface waves between human beings and quadrupeds were encountered. In the trachea of quadrupeds, the mucous surface waves of both the right and left walls fused at the midline of the ventral side and then proceeded in an upward fashion, and those waves of the membranous portion proceeded upward synchronously. In the trachea of human beings, those waves proceeded in a clockwise helical fashion to the oral side. In the main bronchi of them, those waves traveled in a straight, upward fashion. There were no significant differences between the directions of mucous surface waves and mucous flow in any portion of the trachea. When the surface of the specimen was covered with sticky mucous, an abnormal to-and-fro pattern of movement was observed. There was a difference in transport of the foreign bodies and sputum in the large bronchi between human beings and quadrupeds.

Key Words: mucociliary transport, trachea, bronchus, ciliary movement

(*J Bronchol* 2004;11:98–104)

The ventilation of the lung ranges between 1000 and 21,000 L per 24 hours in human beings depending on body size and physical activity.[1] Numerous microparticles of dust and microorganisms are aspirated during ventilation. Mucociliary transport of the airways is regarded as one of the defense mechanisms of the tracheobronchial tree under these conditions. Inhaled particles are entrapped in the mucous layer covering the epithelial surface and then they are continuously removed from the airway by the active beating of cilia.[1–3] We previously reported that real-time images of mucous surface waves and mucous flow could be observed with a stereoscopic zoom microscope system under specific lighting conditions.[4,5] With this system, we investigated directions of mucous surface waves and mucous flow in human beings and quadrupeds, and found large differences between the two, which could have been acquired during the evolution of the large airway defense mechanisms.

MATERIALS AND METHODS

Tracheae, carinae, and main bronchi of 12 human beings, 5 pigs, 3 monkeys, and 1 rabbit were used to investigate the directions of mucous surface waves and mucous flow. Mean age of the human beings examined in this study was 62.8 ± 13.2 years old. There were 6 males and 6 females. Cause of death was cancer in 8 patients, and acute cardiac failure, acute renal failure, cerebral infarction, and interstitial pneumonia in 1 case each. Only 2 of the 12 patients died as a result of respiratory disease. Human specimens were obtained at autopsy, approximately 6 hours after death. These samples were examined after incubation at 37° C in 100% humid air for 20 minutes to simulate conditions in the living body. Animals were anesthetized with sevoflurane and killed with a high dose of intravenous saturated potassium chloride. Animal specimens were obtained and examined immediately after cardiac arrest.

One-centimeter long specimens of the trachea and bronchi were transected and cut at the ventral side. These specimen sections were then opened ventrally and fixed on corkboard as illustrated in Figure 1A. To observe the mucous surface waves on the carina, the outer bilateral sides of the tracheobronchial region were cut and then the specimen sections were opened and fixed on a corkboard as illustrated in Figure 1B. The corkboard was placed on the angle-adjustable mount (SZH-SC; Olympus, Co., Tokyo, Japan) of a stereoscopic zoom microscope (SMZ-U; Nikon Co., Tokyo, Japan) equipped with a fiberoptic light source (Fig. 1C, D). The angle of incidence was adjusted so as to be 25° to 40° to the bronchial surface to observe the specimens from the best vantage point. By changing both the angle of the mount and the direction of the fiberoptic light source variously, the mucous surface waves could be ob-

From the *Department of Thoracic Surgery, Institute of Development, Aging and Cancer, Tohoku University, Seiryomachi, Aoba-ku, Sendai, Japan; and the †Second Department of Surgery, Faculty of Medicine, Kagoshima University, Sakuragaoka, Kagoshima, Japan.

Reprints: Dr. Masami Sato, Department of Thoracic Surgery, Institute of Development, Aging and Cancer, Tohoku University, 4-1 Seiryomachi, Aoba-ku, Sendai 980-8575, Japan (e-mail: m-sato@idac.tohoku.ac.jp).

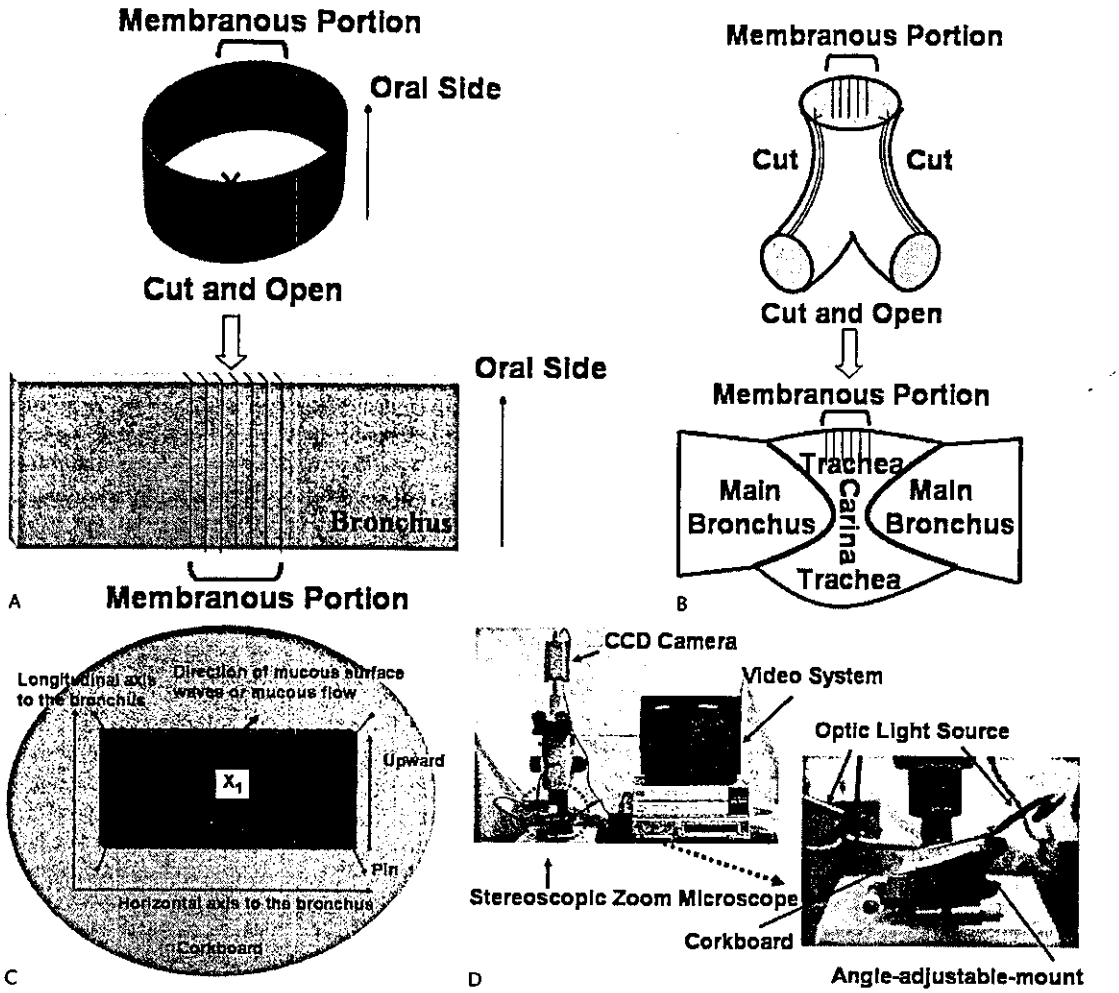

FIGURE 1. Schema of observation method. A, One-centimeter long specimens of the trachea and bronchi were transected and opened at the ventral side. The section was placed so that the membranous portion was central and the oral side was at the top. The angle with respect to the horizontal axis of the airway was measured and investigated. The directions of the mucous surface waves were evaluated using the angle. B, To observe the mucous surface waves on the carina, the outer bilateral sides of the tracheal–broncheal region were cut and then the specimen sections were opened at the bilateral side and fixed on a corkboard. C, Definition of the axis and direction. D, Photograph of the observation system.

served in the area of halation. The image was captured by CCD camera (HV-C20M; Hitachi, Co., Tokyo, Japan), monitored on a 14-inch television monitor and recorded on videotape simultaneously. In addition, 125 frames per second of ciliary images were captured by a high-speed video camera. The stereoscopic zoom microscope magnified the objects up to 500 times for observation of the directions of both mucous surface waves and mucous flow. These observed directions were defined as the angle against the horizontal axis of the airway sections (X_1 in Fig. 1C). Although the directions of mucous surface waves could be observed directly, those of mucous flow could not. Thus, we observed the movement of microparticles of dust or microbubbles on the surface of the mucosa. When we could not find microparticles or microbubbles, saline solution, which had been shaken and contained tiny bubbles, was placed on the surface of the bronchi. The directions of both mucous surface waves and mucous flow were measured at 4 points of each specimen, ie, the left, right, ventral, and dorsal sides of the specimen sections. This protocol was approved by the Ethics Committee of Tohoku University, School of Medicine, in Japan. All data are shown as means ± standard deviation, and all values were analyzed by Student *t* test. When the *P* value was less than 0.05, the values were considered to be significant.

RESULTS

Observation of the Mucous Surface Movement

The visual images of the mucous surface movement were found to change along with the focus of the stereoscopic zoom microscope. We found 3 optimal foci for observing the cilia-related movements. In the deep layer of the large bronchi, the image of the movement resembled a mushroom-like structure (Fig. 2A). In the middle layer of the large bronchi, the image of the movement had a whip-like motion with a regular rhythm. The motion of each structure had a specific direction (Fig. 2B). Finally, mucous surface waves and mucous flow were observed on the surface layer of the large bronchi (Fig. 2C). Figure 2D shows the microbubbles after application of a drop of shaken saline solution. Mucous surface waves were not observed as a result of the interruption of the saline. However, movements of the microdust and/or microbubbles were clearly detectable (Fig. 2E). This direction was thought to be that of mucous flow. There was no difference in mucous surface waves or mucous flow according to age and gender.

Directions of Mucous Surface Waves (human beings vs. pig, monkey, and rabbit)

In the main bronchi of both human beings and pigs, mucous surface waves traveled in a straight fashion (white arrows in Figure 3B, D). In the carina of both human beings and quadrupeds, mucous surface waves propagated in different directions toward either the ventral or dorsal side (black arrows in Fig. 3B, D).

In the trachea of human beings, the directions of mucous surface waves were 133 ± 35° (ventral side), 122 ± 33° (dorsal side), 132 ± 36° (left side), and 126 ± 22° (right side) (Table 1A). There were no significant differences between the directions of mucous surface waves and mucous flow in any portion of the trachea. Moreover, mucous surface waves propagated in the same directions everywhere in the trachea. That is to say, mucous surface waves in the trachea proceeded to the oral side with an inclination of approximately 60° with respect to the horizontal axis of the airway. These results indicated that mucous surface waves proceeded upward in a clockwise helical fashion in human beings (Fig. 3A).

On the other hand, in the quadruped trachea, the directions of mucous surface waves were 92 ± 5° (ventral side), 90 ± 0° (dorsal side), 72 ± 60° (left side), and 118 ± 34° (right side) (Table 1B). In the left and right side of the trachea, the mucous surface waves traveled down the tracheal sidewall ventrally at an inclination of approximately 70° with respect to the longitudinal axis of the airway to the oral side with gravity. These results indicated that the bilateral mucous surface waves fused at the midline of the ventral side and then proceeded orally, and that the mucous surface waves of the membranous portion proceeded upward synchronously in pigs (Fig. 3C).

There were large differences in the directions of mucous surface waves and mucous flow in the trachea between human beings and pigs. Other 4-footed animals (ie, monkey and rabbit) examined in this study also showed results similar as those of pigs.

The Visual Images With Abnormal Movements

Mucous surface waves mentioned here could be observed only when the condition of the specimen was good. Otherwise, there were quite different views of the mucous surface waves (Fig. 4). The surface of the large bronchi glittered when it seemed to be covered with sticky mucous. The mucous surface movement on both the deep and middle layers could not be observed as a result of the reflection of the light. Furthermore, mucous surface waves did not propagate under such condition, and abnormal movement, termed a to-and-fro pattern, was observed in 3 patients.

DISCUSSION

In the present study, we showed that mucous surface waves of human beings moved in a clockwise helical fashion toward the oral side of the trachea, whereas mucous surface waves in quadrupeds fused at the midline of the ventral side of trachea and then proceeded in a straight, upward fashion. We examined mucous surface waves of pigs, monkeys, and a rabbit and found similar findings. These findings indicate that there is a clear distinction in the direction of the tracheal mucous surface waves between human beings and quadrupeds.

In the absence of direct visual measurement of metachronal waves, there have been few reports on metachronal waves of the human trachea. Cruz and colleagues reported the clockwise helical movement of small Teflon discs placed on the surface of the trachea by means of a cine-bronchofiberscope.[6] Wong et al. measured a propagation direction of 36° with respect to the horizontal axis of the canine trachea by a heterodyne mode correlation analysis laser lighting scattering system.[7] In their examinations, they used quite different methods and were not able to observe the metachronal waves directly. However, their results support our findings. In our study, we were able to measure many mucous surface waves at various sites in the trachea and were also able to detect the directions on the visual images, which showed mucous surface wave propagation directions to be 47° to 52° with respect to the horizontal axis of the human trachea. Unfortunately, we could not conclude whether mucous surface waves and mucous flow observed with our methods were the same as those with their methods, because the methods used were different.

Foreign bodies in the trachea must be removed by the mucociliary transport system and/or the cough reflex against gravity. Gravity could play an important role in the mucous flow in human beings. One of the great differences between human beings and quadrupeds is the way of walking, ie, bipe-

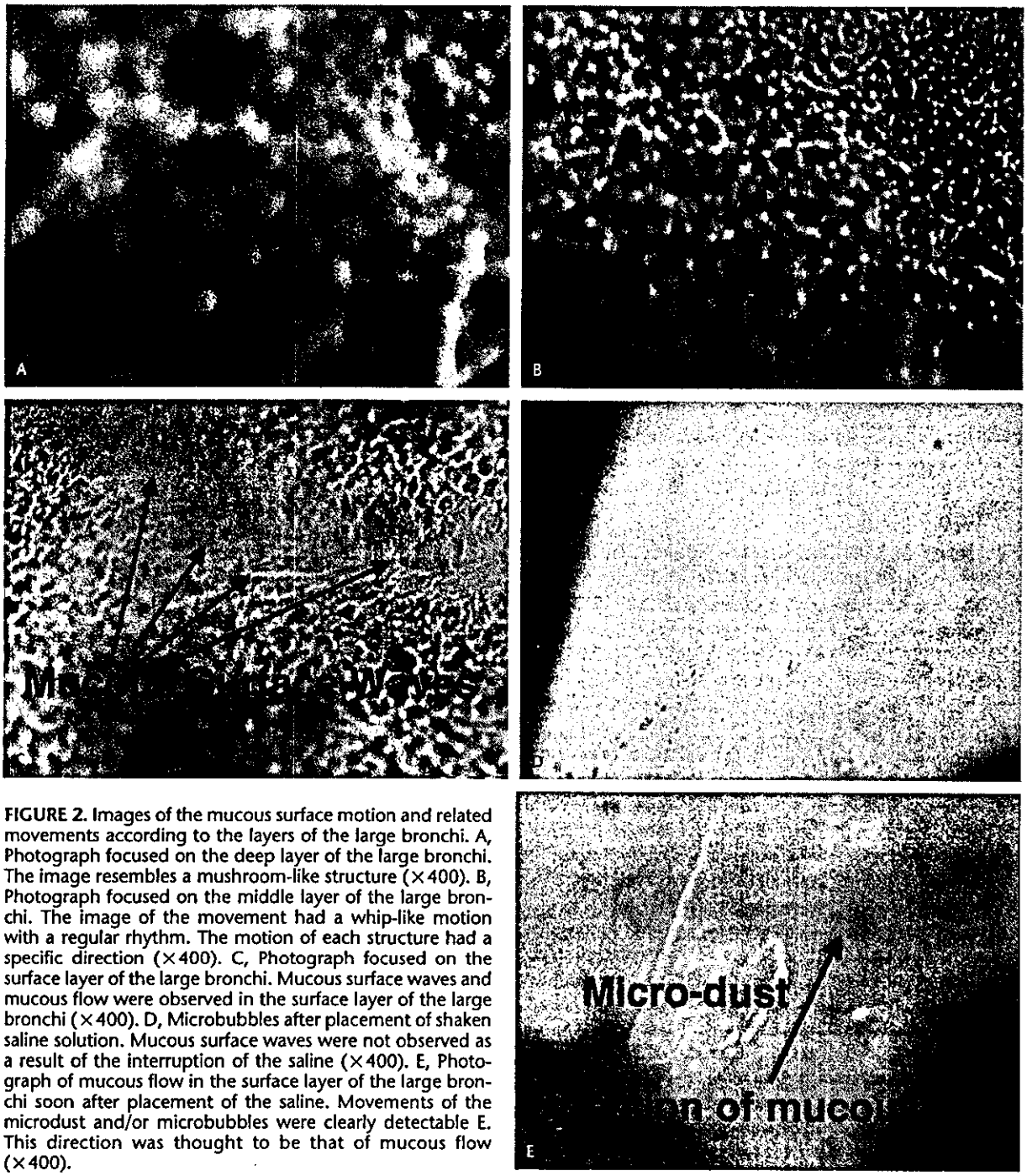

FIGURE 2. Images of the mucous surface motion and related movements according to the layers of the large bronchi. A, Photograph focused on the deep layer of the large bronchi. The image resembles a mushroom-like structure (×400). B, Photograph focused on the middle layer of the large bronchi. The image of the movement had a whip-like motion with a regular rhythm. The motion of each structure had a specific direction (×400). C, Photograph focused on the surface layer of the large bronchi. Mucous surface waves and mucous flow were observed in the surface layer of the large bronchi (×400). D, Microbubbles after placement of shaken saline solution. Mucous surface waves were not observed as a result of the interruption of the saline (×400). E, Photograph of mucous flow in the surface layer of the large bronchi soon after placement of the saline. Movements of the microdust and/or microbubbles were clearly detectable E. This direction was thought to be that of mucous flow (×400).

dal versus quadruped walking. Namely, the human trachea is perpendicularly situated in the body, whereas the trachea of quadrupeds is situated almost horizontally. In quadrupeds such as the pig, sputum is collected at the ventral side of the trachea and is then carried out to the oral side, which seems to be rational from the viewpoint of cooperation with gravity. In human beings, however, such a system might not be effective for transport of the sputum because of the different posture. Larger

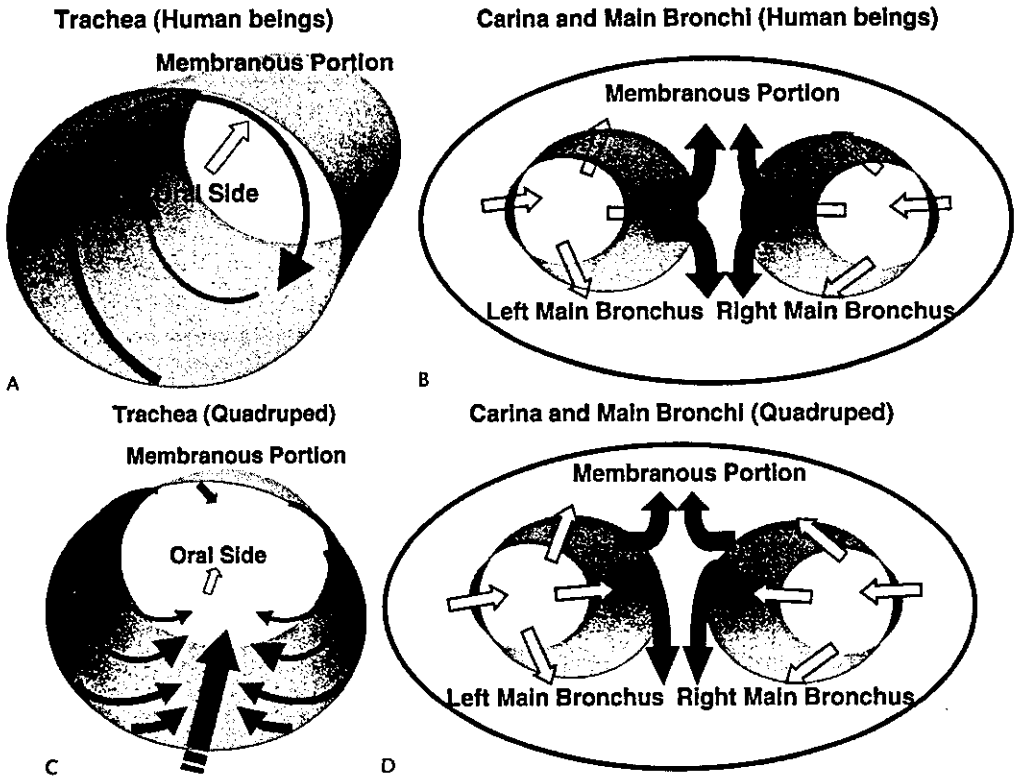

FIGURE 3. A, Schema of mucous surface wave directions in the human trachea. Mucous surface waves proceed upward in a clockwise helical fashion to the oral side. B, Schema of mucous surface wave directions in human carina and main bronchi. Mucous surface waves of the main bronchi travel in a straight, upward fashion, then proceed equally anteriorly and posteriorly on the carina. White arrows: direction of mucous surface waves in the main bronchus. Black arrows: direction of mucous surface waves on the carina. C, Schema of mucous surface wave directions in quadruped trachea. Bilateral mucous surface waves fuse at the midline of the ventral side and then proceed in an upward fashion. In the membranous portion, mucous surface waves proceed upward synchronously. D, Schema of mucous surface wave directions in quadruped carina and main bronchi. Mucous surface waves of the main bronchi proceed straight upward, then divide on the carina as anterior and posterior waves, the majority of the waves occupying the anterior side. White arrows: direction of mucous surface waves in the main bronchus. Black arrows: direction of mucous surface waves on the carina.

force is necessary to carry the foreign body perpendicularly against gravity. Based on the law of energy conservation, slanted mucociliary movement is necessary in human beings because it requires smaller force to carry sputum (Fig. 5). For example, when the angle of a mucous surface wave with respect to the horizontal axis is 45° to 60°, the force necessary for carrying sputum along the slope is $1/\sqrt{2}$ to $\sqrt{3}/2$ of the force, which is necessary for sputum to move straight upward. In fact, human mucous surface waves proceed upward in a clockwise helical fashion. It is considered that this could be 1 of the evolutionary steps from quadrupeds to bipeds. There are some quadrupeds such as the giraffe with long perpendicular necks for which it would be interesting to see how mucous surface waves proceed. Another interesting question is whether the position of the body affects the direction of mucous surface waves. Also, what is the situation in bedridden patients?

An interesting finding is that mucous surface waves traveled along the horizontal axis of the main bronchus in any of the vertebrates we examined. As a result, in human beings, there was a significant difference in the direction of mucous surface waves between the trachea and the main bronchi. In human beings, the main bronchus is situated obliquely, which requires a smaller force to transport substances. If the human main bronchus were located perpendicularly, a larger force would be needed to transport substances along the longitudinal axis against gravity. It might not be necessary for human tracheal transport to proceed in an upward helical fashion. On the other hand, mucous surface waves are divided into the ventral side and the dorsal side in the carina. The ratio of the ventral side to the dorsal side in quadrupeds is larger than that in human beings. This could also be the result of gravity.

TABLE 1. Angle (X_1) of Mucous Surface Wave With Respect to the Horizontal Axis of Trachea and Main Bronchi in Human Beings (A) and Pigs (B) (X_1 in Fig. 1C)

Mucous Surface Wave	Trachea	Main Bronchus
Human beings		
Ventral side	133 ± 35	97 ± 12
Dorsal side	122 ± 33	113 ± 25
Left side	132 ± 36	97 ± 15
Right side	126 ± 22	100 ± 10
		(degrees)
Pigs		
Ventral side	92 ± 5	90 ± 0
Dorsal side	90 ± 0	90 ± 0
Left side	72 ± 60	90 ± 8
Right side	118 ± 34	94 ± 5
		(degrees)

This kind of study has some limitations. Because the human specimens were obtained at autopsy, various medicines as well as physical injuries resulting from tracheal tubes, suction catheters, and bronchoscopes might be causes of unknown effects on ciliary movement. Also, sevoflurane and potassium chloride, which were used in our study, are considered to have some influences on the ciliary beat frequency, mucus secretion, and mucociliary clearance.[1] However, there are no reports that these medicines and physical injuries affect the directions of mucous surface waves.

To our knowledge, this is the first report of a to-and-fro pattern of mucous surface waves. No method other than our original method can detect this phenomenon. The airway ciliary motion of patients with airway diseases such as asthma or bronchitis could show the to-and-fro pattern. The airway epithelium is covered with 2 layers.[8] The upper layer is a gel layer, which consists of mucin secreted from bronchial gland cells and goblet cells. The lower layer is a sol layer containing periciliary fluid, which consists of chloride-water secreted by serous cells.[9] The composition of the surface liquid is changed by many factors.[10,11] Wanner and colleagues reported that cholinergic, α, β-adrenergic, and peptidergic neurotransmitters increase tracheal mucus and water secretion.[1] Moreover, the change in the composition of surface liquid affects both the beating parameters and the degree of ciliary coupling, which would be reflected in the characteristics of metachronal waves.[12,13] Cruz et al. reported that the average mucous velocities were 21.5 mm/min in normal nonsmoker volunteers, 5.5 mm/min in patients with a common cold, and 1.7 mm/min in patients with chronic obstructive lung disease.[6] This report supports the idea that inflammation influences mucociliary transport. Thus, we speculate that in chronic obstructive lung disease, a to-and-fro pattern of mucous surface waves could be seen. A large amount of mucus in the airway is observed in patients with asthma and bronchitis,[14] which would bring about a change in the composition of the surface liquid. The to-and-fro pattern of mucous surface motion is a condition in which the mucociliary transport system does not work well. Our next question is what airway diseases show such a to-and-fro pattern. Bronchial asthma, bronchitis, immotile cilia syndrome, and the air-dried state could be candidates. Further study is needed for clarification and a possible answer to this question.

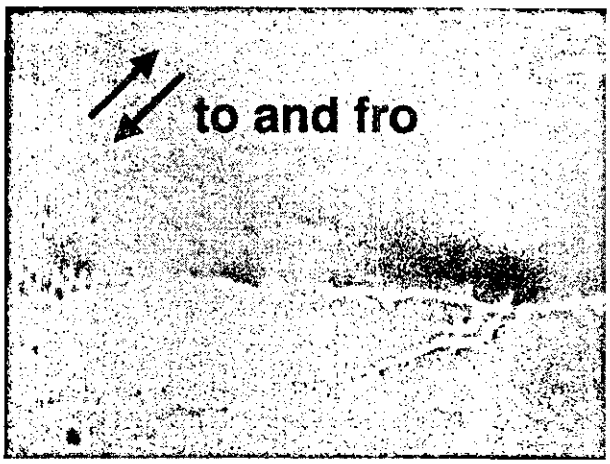

FIGURE 4. Photograph of the to-and-fro pattern of mucous surface waves.

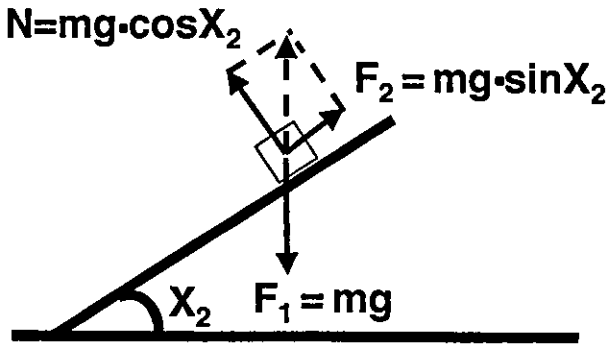

FIGURE 5. Schema of the dynamic balance between the force of the mucous surface waves and gravity in humans. Spiral transportation is useful, because it can carry a larger burden with smaller force. F_t, gravity; F_2, force of mucous surface waves; N, drag; m, mass; g, gravitational acceleration; X_2, 180-X_1, X_1 in Figure 1.

CONCLUSION

Mucous surface wave directions were found to be different between human beings and quadrupeds. In addition, human

mucociliary transport systems were different between the trachea and the main bronchi. All these features could contribute to efficient mucous transportation against gravity. A to-and-fro pattern of mucous surface waves was observed to be an indication of mucociliary transport dysfunction.

REFERENCES

1. Wanner A, Salathe M, Oriordan TG. Mucociliary clearance in the airways. *Am J Respir Crit Care Med.* 1996;154:1868–1902.
2. Sleigh MA, Blake JR, Liron N. The propulsion of mucous by cilia. *Am Rev Respir Dis.* 1988;137:726–741.
3. Seybold ZV, Mariassy AT, Stroh D, et al. Mucociliary interaction in vitro: effects of physiological and inflammatory stimuli. *J Appl Physiol.* 1990; 68:1421–1426.
4. Sakurada A, Sato M, Sagawa M, et al. Real-time observation of the ciliary motion of the bronchial epithelium through a bronchovideoscope. *Bronchology and Bronchoesophagology: State of the Art.* 2001;550–552.
5. Sakurada A, Sato M, Sagawa M, et al. Real-time visualization of ciliary motion on the bronchial surface. *Journal of Bronchology.* 2003;10:30–33.
6. Cruz RS, Landa J, Hirsch J, et al. Tracheal mucous velocity in normal man and patients with obstructive lung disease; effects of terbutaline. *Am Rev Respir Dis.* 1974;109:458–463.
7. Wong LB, Miller IF, Yeates DB. Nature of the mammalian ciliary metachronal wave. *J Appl Physiol.* 1993;75:458–467.
8. Lucas AM, Douglas LC. Principles underlying ciliary activity in the respiratory tract. A comparison of nasal clearance in man, monkey and other animals. *Arch Otolaryngol.* 1934;20:518–541.
9. Widdicombe JH. Ion and fluid transport by airway epithelium. In: Takishima T, Shimura S, et al., eds. *Airway Secretion. Physiological Bases for Control of Mucus Hypersecretion.* New York: Marcel Dekker Inc; 1994:399–432.
10. Mercke U, Hakansson CH, Toremalm NG. The influence of temperature on mucociliary activity: temperature range 20 degrees C to 40 degrees C. *Acta Otolaryngol.* 1974;78:444–450.
11. Mercke U. The influence of temperature on mucociliary activity: temperature range 40°C–50°C. *Acta Otolaryngol.* 1974;78:253–258.
12. Gheber L, Priel Z. Metachronal activity of cultured mucociliary epithelium under normal and stimulated conditions. *Cell Motil.* 1994;28:333–345.
13. Gheber L, Korngreen A, Priel Z. Effect of viscosity on metachrony in mucus propelling cilia. *Cell Motil.* 1998;39:9–20.
14. Shimura S, Andoh Y, Haraguchi K, et al. Continuity of airway goblet cells and intraluminal mucus in the airways of patients with bronchial asthma. *Eur Respir J.* 1996;9:1395–1401.

Laboratory Investigation (2004) 84, 1339–1351
 0023-6837/04 $30.00
www.laboratoryinvestigation.org

Chromosome 12, frequently deleted in human pancreatic cancer, may encode a tumor-suppressor gene that suppresses angiogenesis

Sumitaka Yamanaka[1,2,*], Makoto Sunamura[3,*], Toru Furukawa[1], Libo Sun[3], Liviu P Lefter[1,3], Tadayoshi Abe[1,3], Toshimasa Yatsuoka[1,3], Hiroko Fujimura[3], Emiko Shibuya[3], Noriko Kotobuki[4], Mitsuo Oshimura[4], Akira Sakurada[2], Masami Sato[2], Takashi Kondo[2], Seiki Matsuno[3] and Akira Horii[1]

[1]*Department of Molecular Pathology, Tohoku University School of Medicine, Sendai, Japan;* [2]*Department of Thoracic Surgery, Institute of Development, Aging and Cancer, Tohoku University, Sendai, Japan;* [3]*Department of Gastroenterological Surgery, Tohoku University School of Medicine, Sendai, Japan and* [4]*Department of Cell Technology, Tottori University School of Medicine, Yonago, Japan*

Several lines of evidence have suggested that the long arm of chromosome 12 may carry a tumor-suppressor gene(s) that plays a role in pancreatic ductal carcinogenesis. We have previously found a significant association between loss of heterozygosity of the 12q arm and a poor prognosis in pancreatic cancer patients. In this study, we introduced a normal copy of chromosome 12 into some pancreatic ductal carcinoma cells. Both anchorage-dependent and -independent proliferations as well as invasiveness were similar throughout the hybrid clones when compared with their corresponding parental cells. In sharp contrast, significant suppression of tumorigenesis was observed after inoculation of the hybrid clones into nude mice. Measurements made up to 1 month later showed that there was a significant delay in the growth of tumors into which the introduced normal copy of chromosome 12 had been restored. More significantly, using our dorsal skin chamber and an intravital microscopy system experiment in SCID mice, we demonstrated and visualized directly that implantation of the hybrids failed to promote the angiogenic phenotype encountered in the parental cells. Gene expression profiling using the complementary DNA microarray system identified a set of 24 genes differentially expressed between the hybrids and parental cells. An additional set of 18 genes was also identified that were differentially expressed between the hybrid clone that lost its growth-suppression activity and one that retained such activity. Another set of 25 genes mapped on 12q was detected that showed high expression levels in the hybrid clones retaining growth-suppressive activity. In summary, this study provides the first functional evidence of the existence of an additional tumor-suppressor gene(s) on chromosome 12, whose absence is responsible for the pathogenesis in pancreatic ductal carcinogenesis.
Laboratory Investigation (2004) **84**, 1339–1351, advance online publication, 9 August 2004; doi:10.1038/labinvest.3700160

Keywords: angiogenesis; chromosome 12; pancreatic cancer

Ductal adenocarcinoma is the most frequent malignancy arising in the pancreas. Although the incidence of this disease is only 3.6% of the cancer cases in Japan, the number of cancer deaths caused by this disease accounts for up to 6.4% of the total (http://www.ncc.go.jp/en/statistics/2001/index.html). The mean 5-year survival rate of this disease is poor; it is below 5% in Japan (http://www.mc.pref.osaka.jp/ocr_e/ocr/index.html#survival) and worldwide.[1] This poor prognosis is partly due to the lack of symptoms arising only at the late stage; nearly 80% of pancreatic cancer patients already harbor metastases at the time of diagnosis. Detection of small, resectable cancers would improve the outcome of

Correspondence: Dr M Sunamura, MD, PhD, Department of Gastroenterological Surgery, Tohoku University School of Medicine, 1-1 Seiryo-machi, Aoba-ku, Sendai 980-8574, Japan. E-mail: msun-thk@umin.ac.jp and Dr A Horii, MD, PhD, Department of Molecular Pathology, Tohoku University School of Medicine, 2-1 Seiryo-machi, Aoba-ku, Sendai 980-8575, Japan. E-mail: horii@mail.tains.tohoku.ac.jp.
*These two authors contributed equally to this work.
Received 6 April 2004; revised 16 June 2004; accepted 29 June 2004; published online 9 August 2004

this deadly disease;[2] but the optimal approach to early detection of pancreatic cancer has not yet been established. Thus, acquisitions of efficient approaches for accurate detection at the earliest stages as well as development of efficient methods for treatment are among the tasks with the highest priority in conquering pancreatic cancer.

Tumor-suppressor genes (TSGs) and their products are attractive candidates as molecular targets for early genetic diagnosis because their functional losses should be followed by switching toward a malignant phenotype. Moreover, there is the possibility of inventing valuable techniques for clinical management of this disease by supplementation of the lost functions of TSGs. Despite the continuous progress in molecular biology, the genetic events involved in the initiation and progression of pancreatic ductal adenocarcinoma remain largely unclear. Cytogenetic, allelotype, and somatic cell hybrid studies in human cancers have suggested that chromosome 12 may carry a TSG(s) that plays a role in the carcinogenises of prostate,[3,4] stomach,[5–7] male germ cells,[8] and pancreas.[9–11] Furthermore, we previously demonstrated that 12q-loss of heterozygosity (LOH) is significantly associated with a poor prognosis in patients with pancreatic cancer.[12] *DUSP6* on 12q was found to be inactivated in pancreatic cancer,[13] and introduction of this gene-induced apoptosis.[14] However, no structural abnormality was observed in this gene, and its localization was outside the smallest region of overlap (SRO). Hence, there is a possibility of the localization of an unknown TSG(s) on 12q that is associated with a poor prognosis in pancreatic cancer patients. To address this possibility and to isolate and characterize the TSG(s) on 12q, we first tried to demonstrate the factor on chromosome 12 that harbored tumor-suppressor activity by means of introduction of a normal copy of chromosome 12.

Materials and methods

Cell Lines

The pancreatic cancer cell lines used were PCI-35 and MIAPaCa2; the former is a generous gift from Dr Hiroshi Ishikura at Hokkaido University, and the latter was purchased from the American Type Culture Collection (Manassas, VA, USA). Chromosome 12 was introduced in these cells by the microcell-mediated chromosome transfer (MMCT) method (see below). Cells were cultured according to the protocols of the suppliers. The parental cell lines were previously well mutationally characterized.[15] The normal human fibroblast cell line MRC-5 (American Type Culture Collection) and the mouse A9 cell line (provided by Japanese Cancer Research Resources Bank) were maintained according to the suppliers' protocols. All cells were routinely monitored for Mycoplasma as well as for mouse hepatitis, Sendai, and pneumonia viruses and were consistently negative.

MMCT

MRC-5 fibroblast cells were transfected with pSV2neo plasmid DNA and then selected in DMEM medium containing 400 μg/ml G418 (GibcoBRL, Grand Island, NY, USA). Cell hybrids of G418-resistant human fibroblast cells and mouse A9 cells were fused, selected, and pooled as described elsewhere.[16] MMCT experiments were performed as described[16,17] using as donors A9H(12) hybrids containing an MRC5 human chromosome 12 tagged with a neomycin-resistance gene, thus allowing clonal selection and expansion in medium containing 400 μg/ml of G418. The resulting final hybrids, five stable clones for each recipient, were named as follows: PCI-35H(12)-1 and -2, and MIAPaCa2H(12)-1 through -3, respectively.

Microsatellite Analysis

Genomic DNA from the A9H(12), parental cell lines, their hybrids, and the corresponding nude mice tumors was analyzed with highly polymorphic microsatellite markers, as described previously.[9] A panel of microsatellite markers was selected that spaced at approximately 10-cM intervals along the long arm of chromosome 12 as follows: *D12S1701* (12q12), *D12S88* (12q21), *D12S1719* (12q21), *D12S360* (12q22), *D12S78* (12q23), and *D12S366* (12q24). *D12S336* on 12p was also used as the control for the short arm marker. Nucleotide sequences of the markers and conditions for PCR have been described previously.[18] The PCR products were separated by running in 6% polyacrylamide/8 M urea/32% formamide gel, followed by fixation in 5% acetic acid/5% methanol for 30 min, drying on a 3 mm filter paper (Whatman Inc., Clifton, NJ, USA) and autoradiography. For each marker, two independent PCR amplifications labelling forward and reverse primers, respectively, were carried out to confirm the results.

Fluorescence *In Situ* Hybridization (FISH)

FISH analysis was carried out as previously described.[10] Briefly, the parental cells and their hybrids were prepared in a metaphase spread by hypotonic treatment and fixation in Carnoy's solution. Dual-color FISH was performed by using two different regional probes for 12q21: b605B21 and b759H8.[19] As the corresponding centromere-specific probe, we used α12H8 corresponding to *D12Z3* (purchased from ATCC, Rockville, MD, USA). BAC DNAs were labelled with biotin–16-dUTP (green signals), and the centromeric probe was labelled with digoxigenin–11-dUTP (red signals). Fluores-

cence detection of the signals was performed with antidigoxigenin–tetramethylrhodamine isothiocyanate (TRITC) and avidin–fluorescein isothiocyanate (FITC) (Boehringer Mannheim, Mannheim, Germany) followed by counterstaining using 4′,6-diamino-2 phenylindole (DAPI) in an antifade solution. At least 100 nuclei for every spread were analyzed, and an average TRITC/FITC ratio profile was estimated.

Proliferation Assays

Anchorage-dependent proliferation was monitored by an MTT assay for 5 days in the absence of G418, and a daily proliferation index (PI) was calculated for each parental and corresponding hybrid cell line by the methods described by van Golen *et al.*[20] In all assays, 1000 cells in 100 μl suspension of each cell type were plated and incubated in wells of five flat-bottomed 96-well plates. The conversion of MTT to formazan dye was spectrometrically measured for absorbance at 590 nm using a multiwell plate ImmunoReader System (Molecular Dynamics, Inc., Sunnyvale, CA, USA). All experiments were performed in duplicates of eight and repeated at least twice. For each cell line, the PI was estimated as previously described.[21] Data from two independent experiments were pooled, averaged, and then statistically analyzed.

For anchorage-independent proliferation, 10 000 cells of each parental and hybrid line were plated in 1 ml medium containing 0.3% Bacto-agar (Becton Dickinson, Sparks, MD, USA) with 10% fetal bovine serum (FBS) as an upper layer into 30-mm dishes. Another 1 ml medium with 0.7% Bacto-agar and 10% FBS was used for the bottom layer. Dishes were maintained in a humidified 5% CO_2 atmosphere at 37°C and fed biweekly with 0.3 ml medium. After 21 days, 0.3 ml of 1 mg/ml INT [2-[4-iodophenyl]-3-[4-nitrophenyl]-5-phenyl-2H-tetrazolium chloride) solution (Dojindo Laboratories, Kumamoto, Japan) was added in each dish and further incubated for another 3 h. The viable, red-stained colonies were photographed using a Zeiss microscope (Carl Zeiss, Göttingen, Germany). Both colony number and size were measured and averaged on three randomly chosen photographs from each plate by using public domain NIH1.62 software. Every anchorage-independent growth was assessed in triplicate by two independent experiments.

Tumorigenicity in SCID Mice

Female SCID mice, 5 weeks old, purchased from Clea Japan Inc. (Tokyo, Japan) were maintained under pathogen-free conditions and used in accordance with NIH and Tohoku University Medical School institutional guidelines. Logarithmically growing cells trypsinized from subconfluent monolayers were suspended in medium containing 25% Matrigel Growth Factor Reduced (Becton Dickinson Labware, Franklin Lakes, NJ, USA) at a density of 1×10^7 cells/ml. For each inoculation, 3×10^6 cells in 0.3 ml suspension were injected s.c. into the hind flanks of nude mice. For every pair of cells, inoculations were performed in three mice. The tumor volume was estimated by the formula: $V = 0.4Dd^2$ (V = tumor volume, D = longitudinal diameter, and d = latitudinal diameter) at the time of biweekly measurements. Data from two inde pendent experiments were pooled for statistical analysis.

In Vivo Microscopy

The dorsal transparent chamber and *in vivo* microscopy system are described elsewhere.[22] A total of 1×10^6 cells of either parental cells or their corresponding hybrids were implanted into the mice. Tumor vessel formation was observed for 3 weeks after tumor cell implantation. Images were captured by a CCD camera (TEC-470 Optronics Co., Chelmsford, MA, USA) attached to a microscope (Nikon, Tokyo, Japan), and recorded on a Super VHS video recorder (Victor, Kanagawa, Japan). Finally, the images were analyzed and prepared off-line using Avid VideoShop 3.0.2 (Avid Technology Inc., Tewksbury, MA, USA) and Adobe Photoshop 5.0.2 (Adobe Systems Inc., San Jose, CA, USA) software.

Immunohistochemistry

Resected specimens were fixed with 4% paraformaldehyde solution overnight. After embedding in OCT compound, the specimens were frozen at −80°C. We used 4 μm sections from frozen specimens for immunohistochemical staining. Anti-mouse CD31 antibody (BD Biosciences-Pharmingen, San Diego, CA, USA) diluted 100-fold in PBS was used as the primary antibody and incubated for 1 h at room temperature. Then the peroxidase-conjugated anti-rat IgG antibody (BD Biosciencies-Pharmingen) was used for the secondary antibody reaction and incubated for 30 min at room temperature, followed by a reaction with AEC reagents (Vector Laboratories, Burlingame, CA, USA) for 10 min at room temperature. AEC reagents were used as chromogens, and hematoxylin was used for counterstaining.

Microarray Analysis

Total RNAs were extracted from the cultured hybrids and their corresponding parental cells using an RNeasy Midi Kit (QIAGEN, Valencia, CA, USA), and the messenger RNAs (mRNAs) were refined from the total RNAs with an Oligotex-dt30 mRNA purification kit (TAKARA, Kyoto, Japan) according to the suppliers' protocols. Cy3- and Cy5-labelled

complementary DNA (cDNA) probes for hybridization were prepared from refined mRNAs with a CyScribe First-Strand cDNA Labelling kit and a CyScribe GFX Purification kit (Amersham Biosciences, Piscataway, NJ, USA) according to the supplier's protocols. We used cDNA microarray slides fabricated by spotting 23 040 unique cDNAs purchased from Amersham Biosciences on Type 7 slides using the Gen III Array Spotter (Amersham Biosciences). The cDNAs were selected from UniGene database,[23] including expressed sequence tags (ESTs), and prepared by PCR-amplification with unique primers. The Lucidea Microarray ScoreCard system (Amersham Biosciences) containing 32 control samples including 11 human housekeeping genes and several artificial cDNAs was used for checking dynamic range and variations of signal intensities according to the supplier's instructions. Each cDNA was spotted in duplicate. Each 10 pmol of labelled probes were hybridized by using Automated Slide Processor according to the supplier's instructions (Amersham Biosciences). The hybridized slides were scanned with a GenePix 4000A scanner (Axon Instruments, Union City, CA, USA). The scanned image was converted to intensity values using GenePix Pro software (Axon Instruments). Duplicated hybridization experiments were carried out for all samples to confirm the results. Standardization of signals was carried out by using the Lucida Microarray ScoreCard software according to the supplier's instructions. The standardized data were analyzed using the GeneSpring software (Silicone Genetics, Red Wood City, CA, USA). Interspot normalization was carried out by dividing sample signal values by control channel values. Interslide normalization was carried out by dividing each signal value by median values of 11 housekeeping genes. We selected genes whose expression showed more than 1.5-fold difference, either higher or lower, with a statistical significance of less than 0.05 in probabilities by ANOVA and *t*-test. Significant differences between parental cells and hybrids were accepted to be less than 0.05 by ANOVA and *t*-test as provided in the software. Annotated information about genes was obtained by using the GeneSpider program provided in the software. Grouping of genes according to ontology was carried out by using the GeneOntology program provided in the software.

Reverse Transcription-PCR

Total RNAs extracted from cell pellets were used for reverse transcription reactions with SuperScript II RNase H-reverse transcriptase (Invitrogen, Inc., San Diego, CA, USA) according to the method described previously.[24] For semiquantitative reverse transcription-PCR, concentrations of template cDNAs were adjusted to give the same quantity by *β2-microglobulin* mRNA measured by ethidium bromide staining in agarose gel electrophoresis. Sequences of primer and optimized conditions for reactions are available upon request. For quantitative RT-PCR, we designed specific primers and fluorescence-labelled probes for the *RAB21* with the primer express

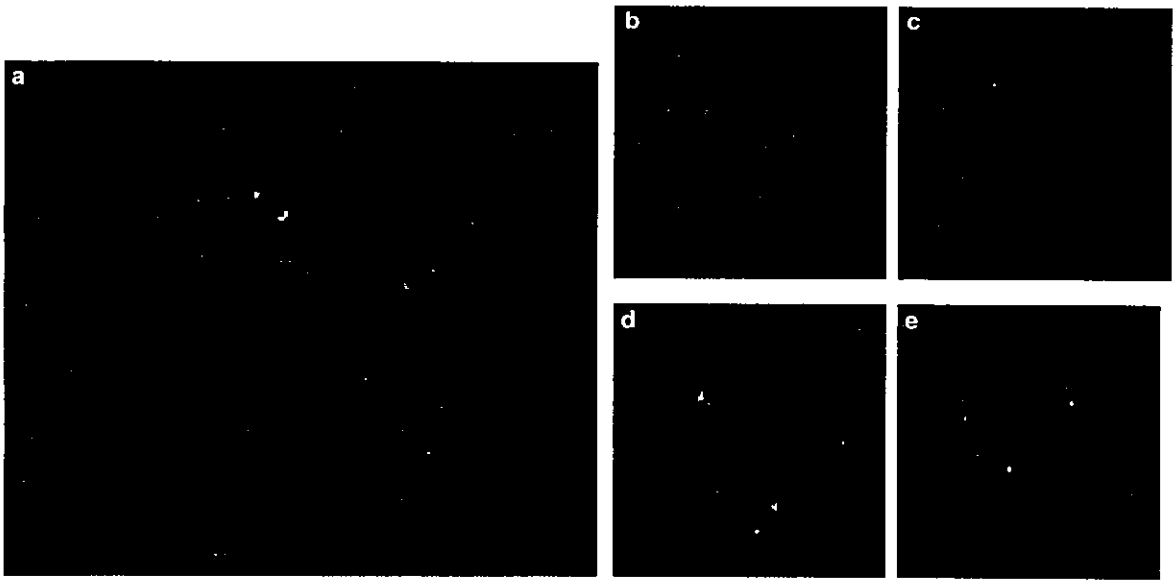

Figure 1 Representative images of FISH analysis for pancreatic cancer cells and their chromosome 12-hybrid clones. Red signals, fluorescence detection with TRITC for the centromere of chromosome 12 (px12H8); green signals, fluorescence detection with FITC for D12S88 localizing at 12q21 (b759H8). (**a**) Chromosome spread of the metaphase of normal cells. (**b–e**) Interphase nuclei of MIAPaCa2 (**b**), MIAPaCa2H(12)-3 (**c**), PCI-35 (**d**), and PCI-35H(12)-1 (**e**).

Table 1 Alteration in copy number detected by FISH

12cen/12q21 ratio[a]	*2/2*	*3/1*	*3/2*	*3/3*	*4/1*	*4/2*	*4/3*	*4/4*	*5/4*	*5/5*
PCI-35	—	—	—	6	—	—	20	***74***	—	—
PCI 35 H(12)-1	—	—	—	10	—	—	30	12	18	***30***
PCI 35 H(12)-2	—	—	—	6	—	—	10	8	30	***46***
MIAPaCa2	6	14	***60***	8	2	8	2	—	—	—
MIAPaCa2 H(12)-1	6	2	14	4	0	22	***38***	—	14	—
MIAPaCa2 H(12)-2	4	16	***31***	2	6	12	29	—	—	—
MIAPaCa2 H(12)-3	8	2	16	8	0	24	***40***	—	2	—

[a]12cen/12q21 ratio was determined by observation of at least 100 nuclei in duplicate.
In each cell line, the most frequently observed 12cen/12q21 ratio is shown in bold italic face.

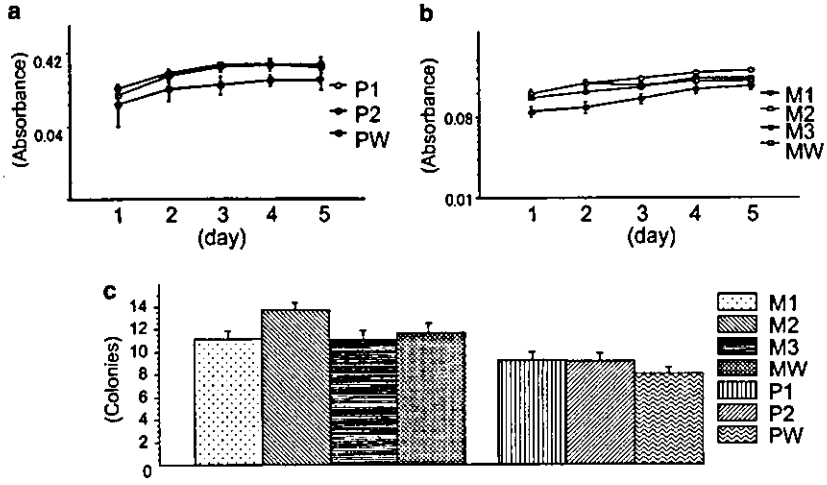

Figure 2 *In vitro* anchorage-dependent proliferation assay. The data were plotted in logarithmic scale. (a) PCI-35 (PW) and PCI-35 hybrid clones (P1 and P2). (b) MIAPaCa2 (MW) and MIAPaCa2 hybrid clones (M1, M2 and M3). (c) *In vitro* anchorage-independent proliferation assay. Each solid bar indicates the number of the colonies in the medium with Bacto-agar after 1 month of culture of cells of PCI-35 (PW), PCI-35 hybrid clones (P1 and P2), MIAPaCa2 (MW), and MIAPaCa2 hybrid clones (M1, M2 and M3).

software (Applied Biosystems, Foster City, CA, USA). Each cDNA was subjected to 40 cycles of the PCR using the ABI PRISM 7700 (Applied Biosystems) according to the supplier's instructions.

Statistical Analysis

All experiments were performed in duplicate or triplicate. A two-tailed Student's *t*-test was performed by using the StatView software 5.0 (SAS Institute Inc., Cary, NC, USA) to determine the statistical significance of differences. The level of significance was established at $P<0.05$.

Results

In this study, we utilized the technique of MMCT to introduce a normal copy of human chromosome 12 individually into two pancreatic cancer cell lines, MIAPaCa2 and PCI-35. In a previous investigation, MIAPaCa2 showed a loss of chromosome 12q arm, whereas PCI-35 did not.[18] We established three independent hybrid clones for MIAPaCa2, MIAPaCa2H(12)-1, -2 and -3, and two independent clones for PCI-35, PCI-35H(12)-1 and -2. To elucidate portions of retained alleles, we performed a microsatellite analysis using a panel of highly polymorphic markers on chromosome 12. However, we could not distinguish between existing alleles and the introduced alleles for most of markers we analyzed because of the few heterozygosities of the microsatellite markers (data not shown). Therefore, we performed a dual-color FISH analysis in duplicate to monitor both the number of introduced chromosomes and the percentage of cells maintaining the introduced chromosome. Markers used were as below: chromosome 12 centromere, 12q21, and 12q23.1. These markers were selected because their high frequencies of losses in primary pancreatic cancer have been reported.[18] Previous works reported that MIAPaCa2 was hypotriploid with losses of 12q21 and 12q23.1, whereas PCI-35 was mainly hypotetraploid without those losses.[18,25] Consistent with the previous results, our FISH analyses, as shown in Figure 1, indicated losses of 12q21

(b759H8) and 12q23.1 (b339F2) in the majority of cells of MIAPaCa2 (Table 1). On the other hand, we found additional signals in the hybrid cells indicating one more copy of portions of the centromere, 12q21 and 12q23.1, as shown in Figure 1; the most frequently observed signal pattern for cen/12q21 or cen/12q23.1 was 3/2 in MIAPaCa2, whereas that in the hybrid was 4/3. Notably, we detected loss of the introduced chromosome in the MIAPaCa2H(12)-2, showing the 3/2 pattern in the majority of cells ($P<0.05$), although the cells maintained resistance to G418. Confirming our previous results,[18] PCI-35 shows an apparently nondefective status of 12q: predominant ratios were 4/4 and 5/5 in parental and PCI-35H(12) cells, respectively. These results are summarized in Table 1. As clearly indicated in Table 1, the hybrid cells we employed were mixed populations of various status of the transferred chromosome because the transferred chromosomes are not stable and sometimes partial loss occurs during the course of serial passages. Each population may express different phenotypes, but we could only observe the mixed phenotypes because of technical difficulties in isolating a pure population.

Once the presence of the introduced chromosome 12 in the hybrids was verified, we estimated their *in vitro* proliferation in either an anchorage-dependent or -independent manner. The results as outlined in Figure 2 show that the *in vitro* growth of the hybrid clones was not significantly different from that of parental cells.

Next, we examined the *in vivo* tumorigenesis phenotypes of the hybrid cells by inoculating them into SCID mice and comparing them with parental cells. In order to shorten tumor latency and enhance tumor growth, we mixed the cells in a suspension containing Matrigel extract. As shown in Figure 3, hybrids MIAPaCa2H(12)-1 and -3 showed significant reductions in tumor volume and a longer latency when compared with their parental cells. MIAPaCa2H(12)-2 and the hybrid clones derived from PCI-35 did not show any significant reduction in tumor volume. Microscopically, tumors generated of the hybrids MIAPaCa2H(12)-1 and -3 tended to form fibrotic changes and showed significant reductions in vessel number as proven by the quantitative vessel counting assay comparing numbers with those in tumors grown from the parental cells (Figure 4). In addition, to compare angiogenesis between MIAPaCa2 and the hybrids, we monitored tumor vessel formation for 3 weeks after tumor cell implantation in a dorsal transparent chamber and an *in vivo* microscopy system. An intense blood vessel formation implying active vascularization

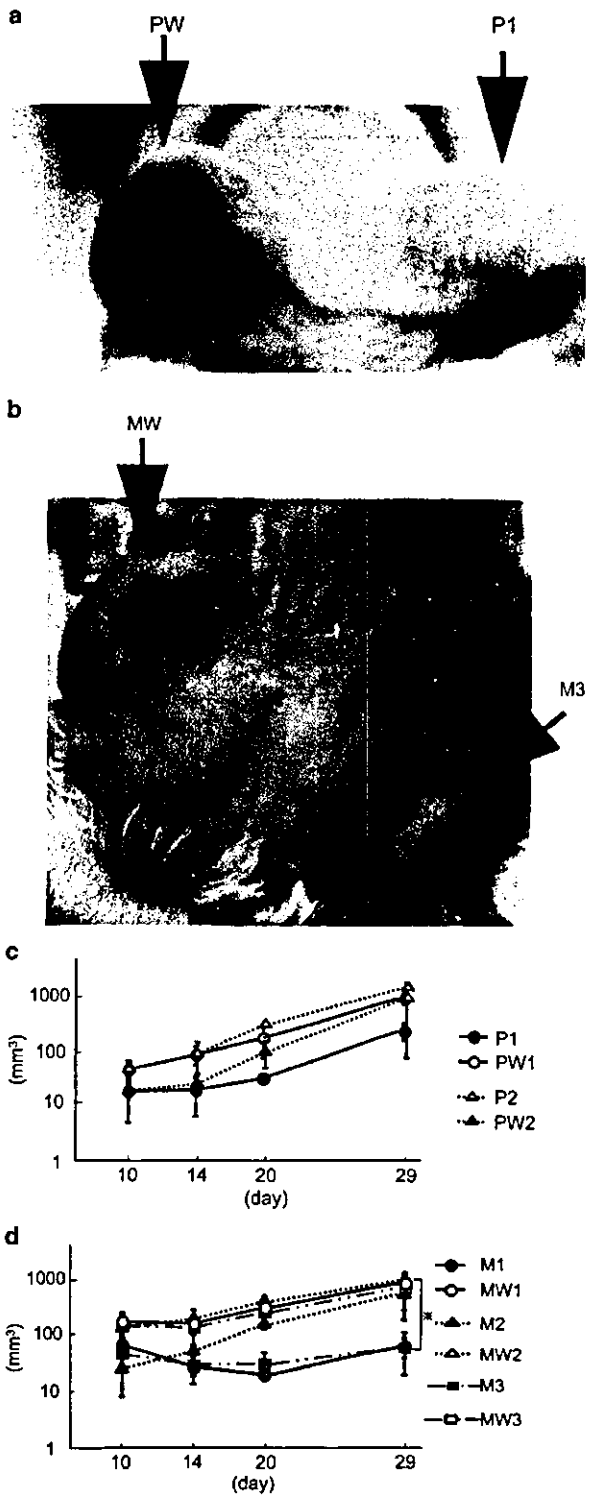

Figure 3 *In vivo* tumorigenic assay employing a total of 3×10^6 tumor cells inoculated into subcutaneum of SCID mice. (a, b) Representative pictures taken at 1 month after the inoculation: (a) PCI-35 (PW1) and PCI-35H(12)-1 (P1), (b) MIAPaCa2 (MW3) and MIAPaCa2H(12)-3 (M3). (c, d) Growth curves of the inoculated tumors. The volume of tumors were plotted in logarithmic scale. (c) PCI-35 clones (PW1 and PW2) and PCI-35 hybrid clones (P1 and P2); (d) MIAPaCa2 clones (MW1, MW2 and MW3) and MIAPaCa2 hybrid clones (M1, M2 and M3). Asterisks denote statistically significant differences ($P<0.05$).